Results in Physics 47 (2023) 106304

Contents lists available at ScienceDirect

Results in Physics

journal homepage: www.elsevier.com/locate/rinp

High-Q quasi-BIC in photonic crystal nanobeam for ultrahigh sensitivity refractive index sensing

Bing Duan [a,1], Songyi Liu [b,1], Xiao Liu [a], Xiao-chong Yu [c], Chuan Wang [d], Daquan Yang [a,e]

[a] State Key Laboratory of Information Photonics and Optical Communications, and School of Information and Communication Engineering, Beijing University of Posts and Telecommunications, Beijing 100876, China
[b] Guangxi Key Laboratory of Optoelectronic Information Processing, School of Optoelectronic Engineering, Guilin University of Electronic Technology, Guilin 541004, China
[c] Applied Optics Beijing Area Major Laboratory, Beijing Normal University, Beijing 100875, China
[d] School of Artificial Intelligence, Beijing Normal University, Beijing 100875, China
[e] School of Information Science and Technology, Tibet University, Lhasa 850000, China

ARTICLE INFO

Keywords:
BIC
One-dimensional photonic crystal nanobeam
quasi-BIC
Refractive index sensing

ABSTRACT

We propose and numerically demonstrate the existence of bound state in the continuum (BIC) in silicon-based one-dimensional photonic crystal nanobeam (1D-PCN). The 1D-PCN is formed by introducing rectangular air nanoholes in a simple 1D nanobeam waveguide. By engineering the structure parameters, an ideal BIC with infinite quality (Q) factor is demonstrated in 1D-PCN. On this basis, we further investigate the refractive index sensing performance with quasi-BIC by introducing defects into the aforementioned 1D-PCN structure, and an ultrahigh Q factor of $\sim 4.1 \times 10^7$ is obtained. Compared to the conventional sensing mechanism based on the shift of forbidden bands modes, the 1D-PCN sensor based on quasi-BIC has a comparable figure of merit (FOM) higher than 10^6. It is worth mentioning that the quasi-BIC can be directly excited by external light sources without the special coupling mechanism, which provides a new method for ultrasensitive refractive index sensing.

Introduction

For the past few decades, the 1D-PCN has attracted great interests for their potential applications in lasing [1], optical sensing [2], filtering [3], modulating [4] and nanoparticle trapping [5], with intriguing features of ultra-compact footprint, easy integration with bus waveguide, and CMOS compatibility. Particularly, the 1D-PCN sensors with various geometries have been designed to achieve ultrahigh FOM, which provides promising platforms for ultrasensitive optical sensing [6–9]. For example, the 1D-PCN sensors have demonstrated the ultrahigh FOMs over 10^5 by designing air modes or introducing a slot structure into dielectric modes [10–14]. Despite their achievements of ultrahigh FOMs, the conventional mechanism of 1D-PCN sensing, for instance, by tracking the shift of forbidden bands modes, usually requires extra couplers (such as fiber lens, grating coupler) and precise nano-positioning systems to assist coupling [15–18].

In contrast, BIC can be directly excited via external light source without special coupling mechanism, providing a new method for ultrasensitive optical sensing. It is a kind of embedded state with an infinite Q factor, and its frequency locates within the radiation continuum [19–23]. In the recent years, BIC has been demonstrated in metasurface, optical waveguide, grating and photonic crystal [24–32], which has facilitated many promising applications, such as the enhancement of nonlinear optical response [33–38], ultrasensitive sensing [39–41], and low threshold laser [42–44]. Although BIC provides an ideal confinement of light in the continuum, it can only exist in theory and is unavailable in practical sensing applications. Quasi-BIC with ultrahigh Q factor provides an alternative for sensing applications, which can be obtained via symmetry-breaking [45–47]. Liu *et al.* have achieved a high FOM over 10^6 based on quasi-BIC mode in coupled bi-layer photonic crystal slabs [46]. Wang *et al.* have reported an asymmetric grating refractive index sensor based on quasi-BIC, demonstrating a FOM higher than 5.1×10^6 [47]. However, the quasi-BIC modes have not been fully explored in 1D-PCN.

In this paper, we report the existence of BIC resonances in 1D-PCN. The Q factors can be tailored in the ranges of hundreds to infinity by

E-mail addresses: wangchuan@bnu.edu.cn (C. Wang), ydq@bupt.edu.cn (D. Yang).
[1] These authors contributed equally to this work.

https://doi.org/10.1016/j.rinp.2023.106304
Received 8 December 2022; Received in revised form 8 February 2023; Accepted 20 February 2023
Available online 4 March 2023

adjusting the incident angles of light. When the incident angle approaches 0°, the BIC with infinite Q factor appears. In order to promote the practical applications of BIC, a quasi-BIC with ultrahigh Q factor of $\sim 4.1 \times 10^7$ is achieved by breaking symmetry. Furthermore, we demonstrate the performance of refractive index sensing by monitoring the shift of quasi-BIC. A high FOM of $\sim 3.2 \times 10^6$ is obtained, which is comparable to the conventional sensing mechanism based on forbidden bands mode shift. The proposed free-space coupled 1D-PCN sensor based on quasi-BIC does not require special coupling mechanism, providing a promising platform for ultrasensitive refractive index sensing.

BIC of 1D photonic crystal nanobeam

Fig. 1 illustrates the schematic of 1D-PCN. It is formed by introducing rectangular air holes ($n_{air} = 1.0$) of length l and width w into a silicon ($n_{si} = 3.575$) ridge waveguide with width of 800 nm ($w_{nb} = 800$ nm). As shown in Fig. 1(a), the incident angle (θ) of plane wave is defined as the propagation direction of the incident light, which represents the angle between the incident beam and y-axis. Fig. 1(b) shows the top view of 1D-PCN. The period p is defined as the distance between the neighboring holes, N is the number of air holes, and the thickness of the silicon waveguide is 220 nm. The optimized structural parameters of 1D-PCN are determined as follows: $l = 500$ nm, $w = 100$ nm, $p = 400$ nm, $N = 5$. Based on the Lumerical FDTD platform, the BIC modes of 1D-PCN are simulated by using the broadband fixed-angle source technique (BFAST). The boundary condition in x-direction is set as bloch period, while the y- and z-directions are set as perfectly matched layer (PML).

Fig. 2 shows the transmission spectra of 1D-PCN at $\theta = 5°$ and $\theta = 0°$ for plane-wave incidence. The transmission spectra exhibit a wide range of high and low transmittance, which accommodate many sharp resonance features. The four resonances in regions I, II, III and IV reveal the vanishing linewidth (black line) as θ is 0°, which are BIC, as shown in Fig. 2(a). When the incident angle of the plane wave is 5°, the transmission spectra exhibit the sharp resonance characteristics (red line) due to the mode leaking out and coupling to the radiation domain. Fig. 2(b) is the enlarged views of regions I, II, III, and IV, respectively, and the vanishing linewidth is evidently observed.

We further investigate the resonant wavelength dependence on incident angles in IV region with the wavelength ranging from 1347 nm to 1377 nm. Fig. 3(a) shows the wavelength variation as the incident angle increases from $\theta = -8°$ to 8°. As depicted in the black dashed box of Fig. 3(a), the resonance disappears when the incident angle is closer to 0°, which demonstrates the BIC and ultrahigh Q factor resonances. Without the consideration of material loss, the Q factor of BIC resonance can approach infinity. To illustrate these phenomena in detail, the transmission spectra near the BIC state are calculated when the incident angles are 0°, 0.3°, 1.0°, 2.0°, and 5.0°, respectively, as shown in Fig. 3 (b). It can be seen that the resonant linewidth becomes narrower when the incident angle gradually decreases from $\theta = 5.0°$ to 0.0°. Finally, the linewidth disappears at $\theta = 0°$, and a BIC is excited. In addition, the resonant wavelength experiences redshift with the increasing of incident angles. Fig. 3(c) shows the electric field distribution when the incident angle is 0.1° and the corresponding resonant wavelength is 1357.57 nm. It is obvious that the 1D-PCN is axisymmetric along the x-axis and y-axis. Therefore, when a plane wave is incident vertically on the structure, the structure is excited and leaky radiation waves from modes interfere and are cancelled by each other. So there are no any radiation loss from the whole structure, and the BIC with an infinitely high Q appears. However, the linewidth of BIC state tends to zero infinitely, we cannot observe it from the transmission spectrum.

By inclining the incident plane wave, the BIC is tuned into quasi-BIC. The Q factors of quasi-BICs at different incident angles are characterized, as shown in Fig. 4. The Q factor is defined as $Q = \lambda_{res}/\delta\lambda$, where λ_{res} is the resonant wavelength, $\delta\lambda$ is linewidth. Note that the Q factor exhibits an inverse square dependence on incident angles (red line), and exceeds 10^6 as the incident angle $\theta = 0.1°$. However, the ideal BIC can only exist in theory and is inaccessible in practical applications. The quasi-BIC resonance with an ultrahigh Q factor provides an alternative in practical applications.

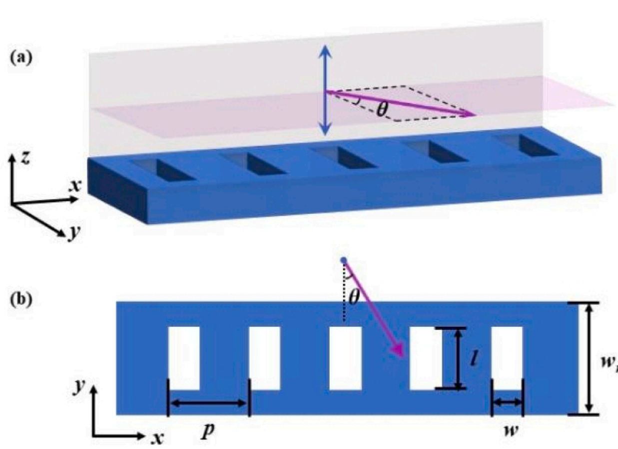

Fig. 1. (a) Schematic of the silicon-based one-dimensional photonic crystal nanobeam (1D-PCN). The incident plane of x-z is shaded grey, and the purple arrow shows the incident wave. (b) Top view of the 1D-PCN in (a). Here, the number of rectangular air holes is $N = 5$, the length and width of air holes are $w = 100$ nm and $l = 500$ nm, respectively, the periodicity $p = 400$ nm, the width of the 1D-PCN is $w_{nb} = 800$ nm, and the thickness of the silicon waveguide is 220 nm.

Quasi-BIC for refractive index sensing

To achieve ultrahigh Q quasi-BIC resonance, we introduce defects into the aforementioned 1D-PCN structure, which is symmetric with respect to the center, as shown in Fig. 5(a). The lengths of rectangular air holes are decreased linearly from center ($l_{center} = 500$ nm) to the both sides, i.e., $l_i = l_{center}\text{-}i\alpha_l$ (i increases from 1 to (N-1)/2), while the periodicity p, hole width w and the number of air holes N are constant. Here, the α_l is defined as an asymmetric parameter. Fig. 5(b) shows the transmission spectra of 1D-PCN at $\alpha_l = 10$ nm and $\alpha_l = 0$ nm. It is observed that only one wide spectrum appears at $\alpha_l = 0$ nm, suggesting the BIC state. The resonance is excited near 1050 nm when $\alpha_l = 10$ nm and the BIC state is turned to the ultrahigh Q quasi-BIC, which can be fitted by a Fano lineshape [48]:

$$T = 1 - M\frac{(x+\alpha)^2}{(x^2+1)(1+\alpha^2)} \tag{1}$$

where M is constant, α is the asymmetric parameter, $x = 2(f\text{-}f_0)/\Delta f$, f_0 is the resonant frequency, Δf is the linewidth of resonance. To elaborate this phenomenon, we further plot the transmission spectra at different α_l, as shown in Fig. 5(c). A redshift of the quasi-BIC is observed when α_l increases from 20 nm to 40 nm with steps of 5 nm, exhibiting the strong dependence of resonant wavelength on α_l. The near-field distribution in x-y plane of the 1D-PCN at $\alpha_l = 20$ nm is plotted in Fig. 5(d). Compared with Fig. 3 (c), the symmetry of the field distribution is broken, which is mainly owing to the introduction of defects in the 1D-PCN. The Q factor increases from 2161.51 to 4.1×10^7 when α_l decreases from 50 nm to 1 nm, as shown in Fig. 6. Therefore, the 1D-PCN can support quasi-BIC with ultrahigh Q factor by introducing defects, providing a feasible platform for ultrasensitive optical sensing and detection.

Finally, we implement the refractive index sensing by monitoring the shift of quasi-BIC. Here, the FOM of refractive index sensor is defined as FOM $= S{\cdot}Q/\lambda_{res}$, where S and Q are the sensitivity and quality factor of the 1D-PCN, respectively, λ_{res} is the resonant wavelength. The Q factor of the quasi-BIC used for refractive index sensing is 4.1×10^7, and the resonant wavelength is 1048.26 nm ($n_{air} = 1.0$). The transmission

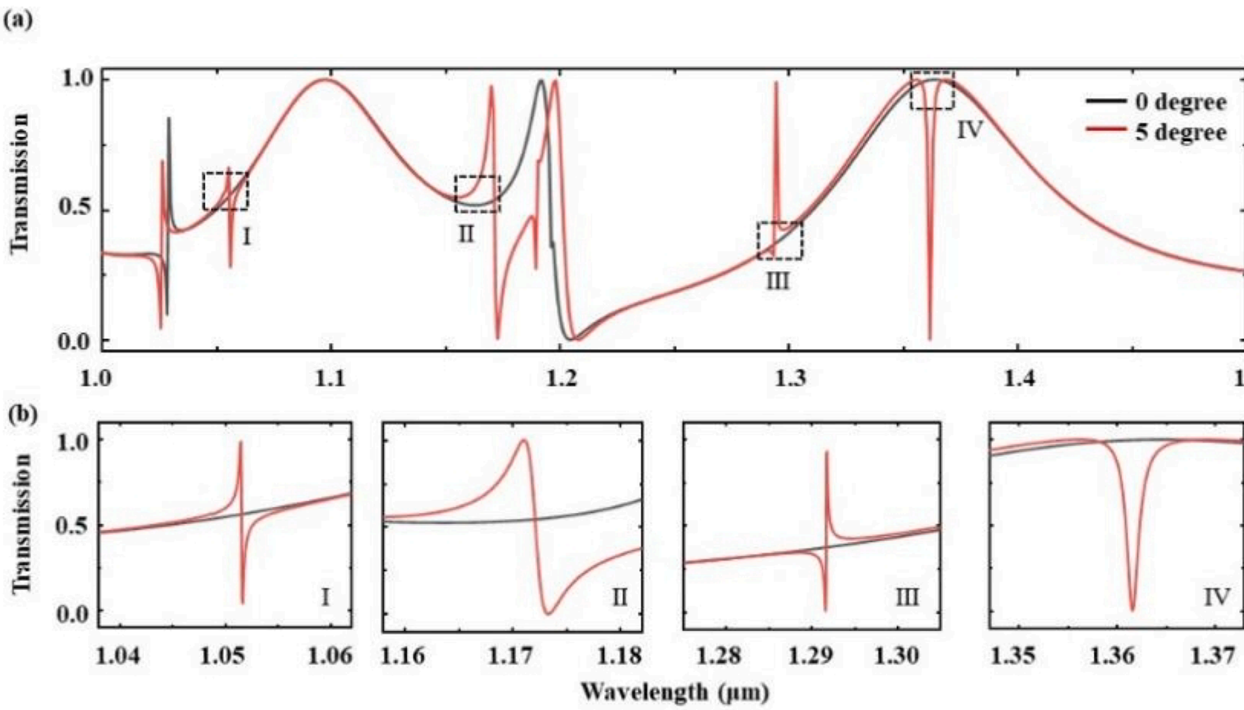

Fig. 2. (a) Transmission spectra with incident angle of 0° and 5°. (b) The enlarged transmission spectra of regions I, II, III and IV, respectively.

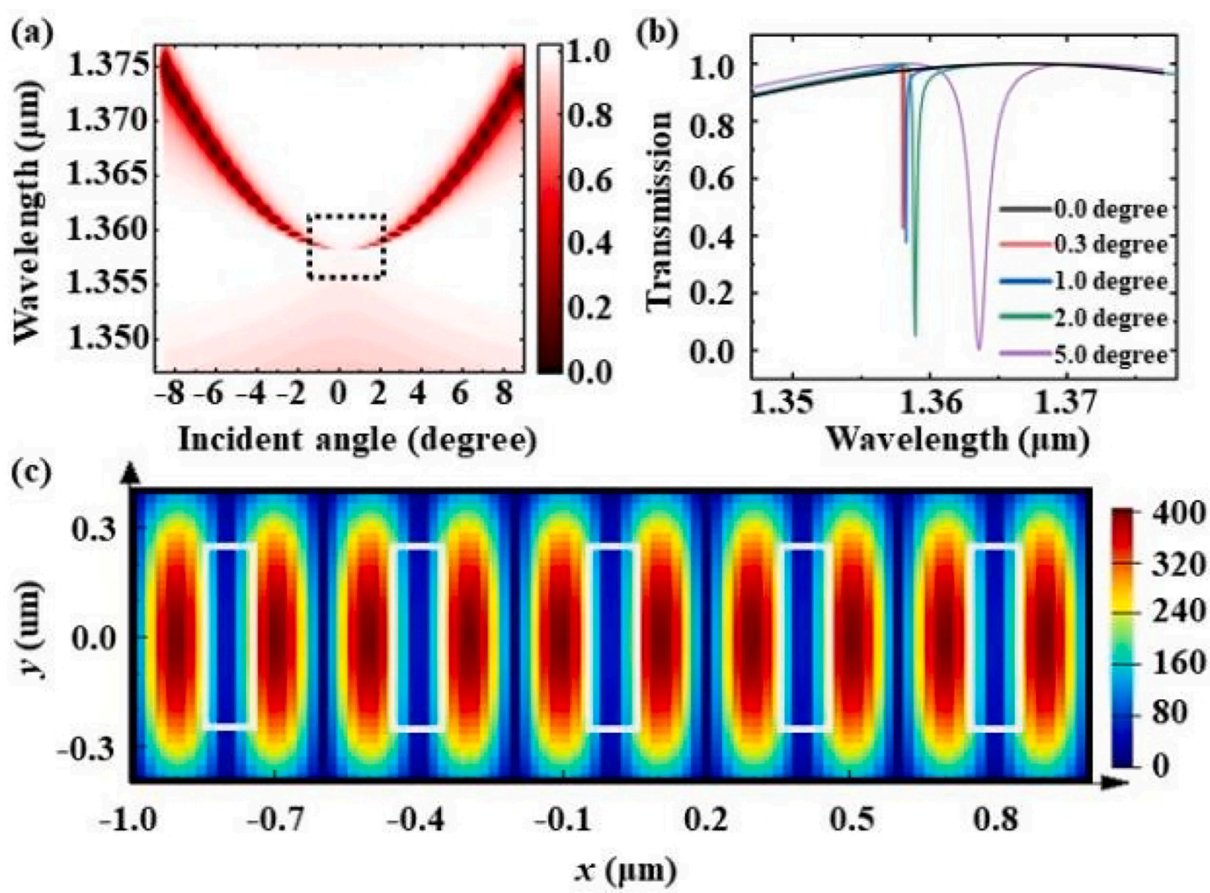

Fig. 3. (a) Transmission spectra in the wavelength ranges of 1347 to 1377 nm when the incident angles rang from − 8° to 8°. (b) Transmission spectra when θ is 0°, 0.3°, 1°, 2°, and 5°. (c) Near-field distributions at $\lambda = 1357.57$ nm and $\theta = 0.1°$ in x-y plane at the center of the silicon layer from 3D-FDTD simulation ($z = 0$).

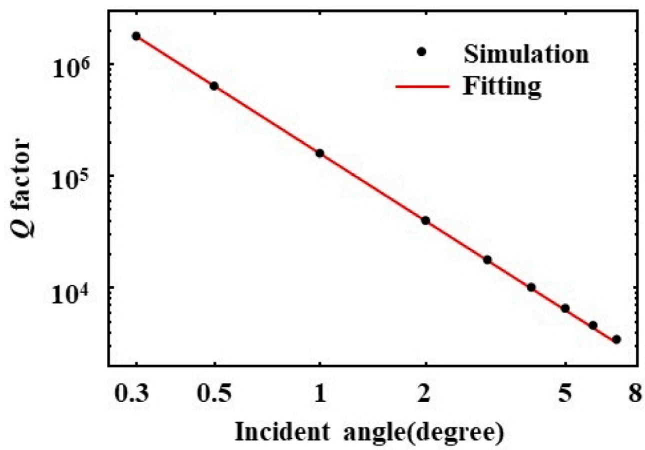

Fig. 4. The dependence of Q factors of the resonances in IV region on incident angles.

evolution is shown in Fig. 7 (a). It is observed that the resonant wavelength suffers redshift with the increment of refractive index. Fig. 7(b) shows the linear dependence of resonant wavelength shifts on refractive index and the sensitivity of 83.3 nm/RIU is obtained. The calculated FOM of the free-space coupled 1D-PCN sensor based on quasi-BIC is 3.2

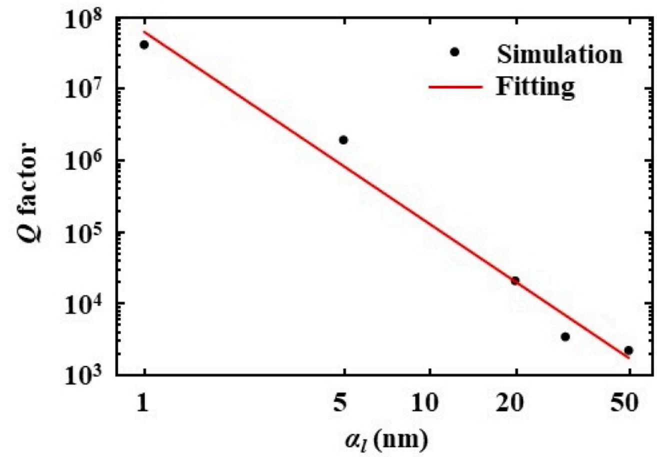

Fig. 6. Q factors of resonances as a function of asymmetry parameters α_l.

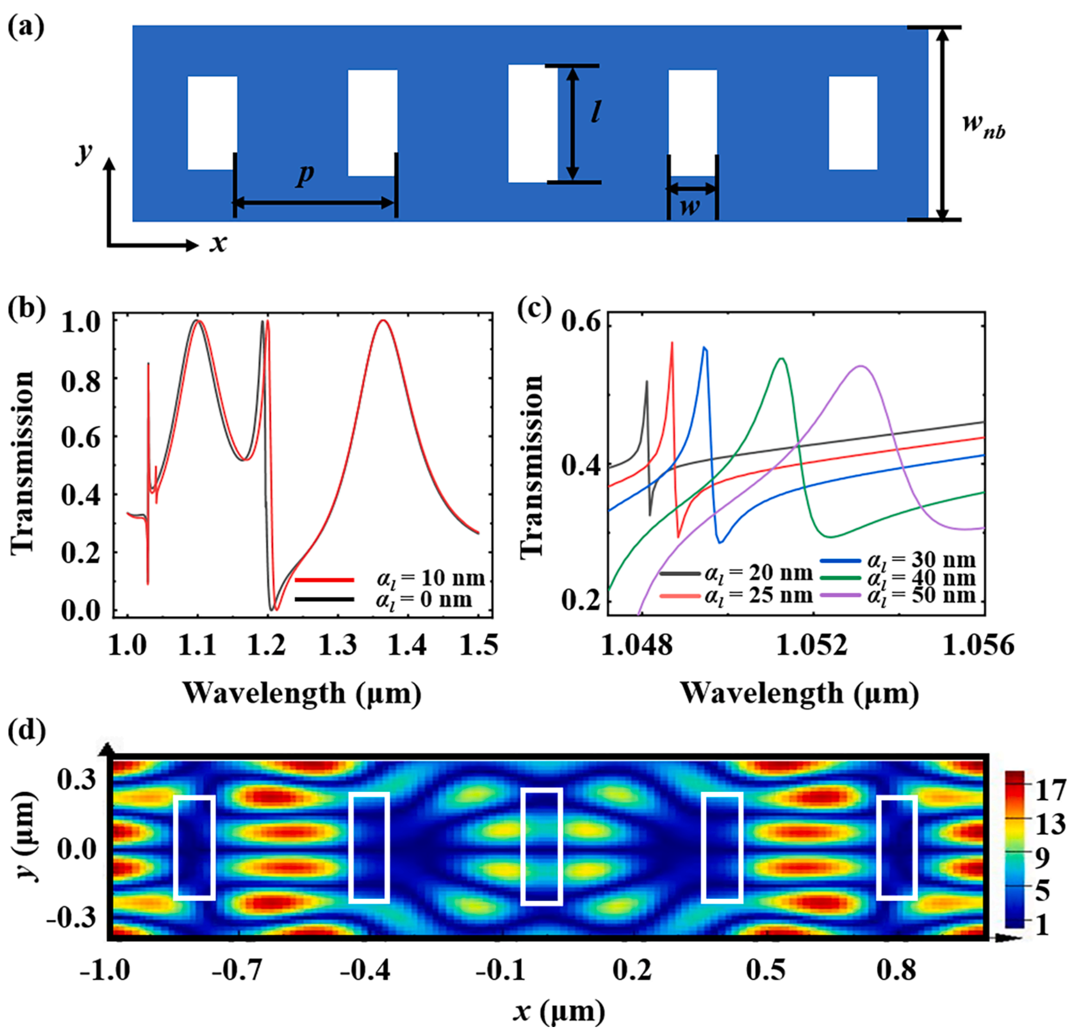

Fig. 5. (a) Schematic illustrations of the 1D-PCN structure with defects. (b) Transmission spectra with α_l of 0 nm and 10 nm when θ is 0°. (c) Transmission spectra for different α_l when θ is 0°. (d) Near-field distributions at $\alpha_l = 20$ nm in the x-y plane.

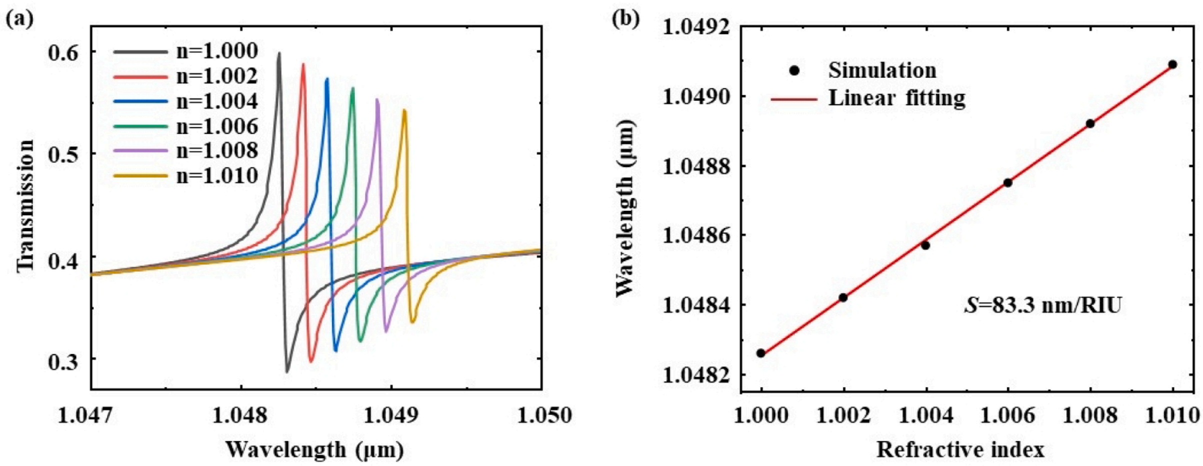

Fig. 7. (a) Transmission evolution of the proposed 1D-PCN sensor when the background refractive index changes from $n = 1.000$ to $n = 1.010$ for $\alpha_l = 1$ nm. (b) The resonant wavelength of 1D-PCN sensor as a function of refractive index.

$\times$ 10^6, which is comparable to the conventional 1D-PCN sensors based on the shift of forbidden bands mode.

Conclusion

In summary, we numerically demonstrate the existence of BIC resonance in silicon-based 1D-PCN. The Q factor is tailored in a wide range of hundreds to infinity by simply tuning the incident angle of the plane wave. When the incident angle of plane wave is 0°, the BIC with infinite Q factor is excited. Furthermore, the BIC state is transferred to quasi-BIC by introducing defects into the 1D-PCN structure. To illustrate the sensing performance of the 1D-PCN sensors based on the quasi-BIC, we investigate the dependence of resonant wavelength on refractive index of the surrounding medium. By using the 3D-FDTD method, a quasi-BIC with ultrahigh Q factor of 4.1×10^7 is used for refractive index sensing, and FOM of 3.2×10^6 is achieved, which is comparable to the conventional sensing mechanism based on the forbidden bands mode shift. It is worth noting that the 1D-PCN sensor based on quasi-BIC does not require special coupling mechanism, providing a new method for the ultrasensitive refractive index sensing. Furthermore, this work exhibits the potential for many applications requiring ultrahigh Q factor, such as ultrasensitive optical sensors, nonlinear photonic hypersurface and low threshold laser.

Funding

This work was supported by National Natural Science Foundation of China [11974058, 62131002, 12104059]; Beijing Nova Program [Z201100006820125] from Beijing Municipal Science and Technology Commission; Beijing Natural Science Foundation [Z210004]; and State Key Laboratory of Information Photonics and Optical Communications [IPOC2021ZT01], BUPT, China; and BUPT Excellent Ph.D. Students Foundation [CX2022114].

Declaration of Competing Interest

The authors declare that they have no known competing financial interests or personal relationships that could have appeared to influence the work reported in this paper.

Data availability

Data will be made available on request.

References

[1] Li YZ, Zhang JX, Huang DD, Sun H, Fan F, Feng JB, et al. Room-temperature continuous-wave lasing from monolayer molybdenum ditelluride integrated with a silicon nanobeam cavity. Nat Nanotech 2017;12:987.
[2] Liu W, Yan J, Shi Y. High sensitivity visible light refractive index sensor based on high order mode Si_3N_4 photonic crystal nanobeam cavity. Opt Express 2017;25: 31739–45.
[3] Pan T, Qiu CY, Wu JY, Jiang X, Liu B, Yang Y, et al. Analysis of an electro-optic modulator based on a graphene-silicon hybrid 1D photonic crystal nanobeam cavity. Opt Express 2015;23:23357–64.
[4] Ge X, Shi Y, He S. Ultra-compact channel drop filter based on photonic crystal nanobeam cavities utilizing a resonant tunneling effect. Opt Lett 2014;39:6973–6.
[5] Yang DQ, Gao F, Cao QT, Wang C, Ji YF, Xiao YF. Single nanoparticle trapping based on on-chip nanoslotted nanobeam cavities. Photon Res 2018;6:99–107.
[6] Rodriguez AG, Markov P, Cartwright AP, Choudhury MH. Photonic crystal nanobeam biosensors based on porous silicon. Opt Express 2019;27:9536–49.
[7] Kim S, Kim HM, Lee YH. Single nanobeam optical sensor with a high Q-factor and high sensitivity. Opt Lett 2015;40:5351–4.
[8] Liang F, Guo YZ, Hou SC, Quan QM. Photonic-plasmonic hybrid single-molecule nanosensor measures the effect of fluorescent labels on DNA-protein dynamics. Sci Adv 2017;3:e1602991.
[9] Yang DQ, Duan B, Liu X, Wang AQ, Li XG, Ji YF. Photonic crystal nanobeam cavities for nanoscale optical sensing: A review. Micromachines 2020;11:72.
[10] Huang L, Zhou J, Sun F, Fu Z, Tian H. Optimization of one dimensional photonic crystal elliptical-hole low-index mode nanobeam cavities for on-chip sensing. J Lightwave Technol 2016;34:3496–502.
[11] Gao Y, Dong PH, Shi YC. Suspended slotted photonic crystal cavities for high-sensitivity refractive index sensing. Opt Express 2020;28:12272–8.
[12] Wang C, Quan Q, Kita S, Li Y, Lončar M. Single-nanoparticle detection with slot-mode photonic crystal cavities. Appl Phys Lett 2015;106:261105.
[13] Xu P, Yao K, Zheng J, Guan X, Shi Y. Slotted photonic crystal nanobeam cavity with parabolic modulated width stack for refractive index sensing. Opt Express 2013;21: 26908–13.
[14] Yang DQ, Chen X, Zhang X, Lan C, Zhang Y. High-Q, low-index-contrast photonic crystal nanofiber cavity for high sensitivity refractive index sensing. Appl Opt 2018;57:6958–9.
[15] Liu PH, Shi YC. Simultaneous measurement of refractive index and temperature using cascaded side-coupled photonic crystal nanobeam cavities. Opt Express 2017;25:28398–406.
[16] Zhang Y, Liu P, Zhang S, Liu W, Chen J, Shi YC. High sensitivity temperature sensor based on cascaded silicon photonic crystal nanobeam cavities. Opt Express 2016; 24:23037–43.
[17] Liang F, Quan QM. Detecting single gold nanoparticles (1.8 nm) with ultrahigh-Q air-mode photonic crystal nanobeam cavities. ACS Photonics 2015;2:1692–7.
[18] Yang DQ, Kita S, Liang F, Wang C, Tian HP, Ji YF, et al. High sensitivity and high Q-factor nanoslotted parallel quadrabeam photonic crystal cavity for real-time and label-free sensing. Appl Phys Lett 2014;105:063118.
[19] Molina MI, Miroshnichenko AE, Kivshar YS. Surface bound states in the continuum. Phys Rev Lett 2012;108:070401.
[20] Romano S, Zito G, Manago S, Calafiore G, Penzo E, Cabrini S, et al. Surface-enhanced Raman and fluorescence spectroscopy with an all-dielectric metasurface. J Phys Chem C 2018;122:19738–45.
[21] Plotnik Y, Peleg O, Dreisow F, Heinrich M, Nolte S, Szameit A, et al. Experimental observation of optical bound states in the continuum. Phys Rev Lett 2011;107: 183901.
[22] Hsu CW, Zhen B, Stone AD, Joannopoulos JD, Soljačić M. Bound states in the continuum. Nat Rev Mater 2016;1:16048.

[23] Penzo E, Romano S, Wang Y, Dhuey S, Dal Negro L, Mocella V, et al. Patterning of electrically tunable light-emitting photonic structures demonstrating bound states in the continuum. J Vac Sci Technol, B: Nanotechnol Microelectron: Mater, Process, Meas, Phenom 2017;35:06G401.

[24] Koshelev K, Bogdanov A, Kivshar Y. Meta-optics and bound states in the continuum. Sci Bull 2019;64:836–42.

[25] Koshelev K, Favraud G, Bogdanov A, Kivshar Y, Fratalocchi A. Nonradiating photonics with resonant dielectric nanostructures. Nanophotonics 2019;8:725–45.

[26] Zito G, Romano S, Cabrini S, Calafiore G, DeLuca AC, Penzo E, et al. Observation of spin-polarized directive coupling of light at bound states in the continuum. Optica 2019;6:1305–12.

[27] Liang Y, Koshelev K, Zhang F, Lin H, Lin S, Wu J, et al. Bound states in the continuum in anisotropic plasmonic metasurfaces. Nano Lett 2020;20:6351–6.

[28] Xu H, Shi Y. Silicon-waveguide-integrated high-quality metagrating supporting bound state in the continuum. Laser & Photonics Rev 2020;14:1900430.

[29] Gao X, Zhen B, Soljacic M, Chen H, Hsu CW. Bound states in the continuum in fiber Bragg gratings. ACS Photonics 2019;6:2996–3002.

[30] Taghizadeh A, Chung IS. Quasi bound states in the continuum with few unit cells of photonic crystal slab. Appl Phys Lett 2017;111:031114.

[31] Ovcharenko AI, Blanchard C, Hugonin JP, Sauvan C. Bound states in the continuum in symmetric and asymmetric photonic crystal slabs. Phys Rev B 2020;101:155303.

[32] Hsu CW, Zhen B, Lee J, Chua S-L, Johnson SG, Joannopoulos JD, et al. Topologically enabled ultrahigh-*Q* guided resonances robust to out-of-plane scattering. Nature 2013;499:188.

[33] Azzam SI, Kildishev AV. Photonic bound states in the continuum: from basics to applications. Adv Opt Mater 2021;9:2001469.

[34] Yu Z, Sun X. Acousto-optic modulation of photonic bound state in the continuum. Light Sci Appl 2020;9:1.

[35] Bezus EA, Bykov DA, Doskolovich LL. Bound states in the continuum and high-*Q* resonances supported by a dielectric ridge on a slab waveguide. Photon Res 2018;6:1084–93.

[36] Bulgakov EN, Maksimov DN, Semina PN, Skorobogatov SA. Propagating bound states in the continuum in dielectric gratings. J Opt Soc Am B 2018;35:1218–22.

[37] Joseph S, Sarkar S, Khan S, Joseph J. Exploring the optical bound state in the continuum in a dielectric grating coupled plasmonic hybrid system. Adv Opt Mater 2021;9:2001895.

[38] Carletti L, Koshelev K, De Angelis C, Kivshar Y. Giant nonlinear response at the nanoscale driven by bound states in the continuum. Phys Rev Lett 2020;121:033903.

[39] Romano S, Lamberti A, Masullo M, Penzo E, Cabrini S, Rendina I, et al. Optical biosensors based on photonic crystals supporting bound states in the continuum. Materials 2018;11:526.

[40] Jin J, Yin X, Ni L, Soljačić M, Zhen B, Peng C. Topologically enabled ultrahigh-*Q* guided resonances robust to out-of-plane scattering. Nature 2019;574:501–4.

[41] Maksimov DN, Gerasimov VS, Romano S, Polyutov SP. Refractive index sensing with optical bound states in the continuum. Opt Express 2020;28:38907–16.

[42] Yu Y, Sakanas A, Zali AR, Semenova E, Yvind K, Mørk J. Ultra-coherent Fano laser based on a bound state in the continuum. Nat Photonics 2021;15:758–64.

[43] Kravtsov V, Khestanova E, Benimetskiy FA, et al. Nonlinear polaritons in a monolayer semiconductor coupled to optical bound states in the continuum. Light Sci Appl 2020;9:56.

[44] Hwang MS, Lee HC, Kim KH, Jeong KY, Kwon SH, Koshelev K, et al. Ultralow-threshold laser using super-bound states in the continuum. Nat Commun 2017;12:4135.

[45] Liu W, Liang Z, Qin Z, Shi X, Yang F, Meng D. Polarization-insensitive dual-band response governed by quasi bound states in the continuum for high-performance refractive index sensing. Results Phys 2022;32:105125.

[46] Liu C, Bai Y, Zhou J, Chen J, Qiao L. Refractive index sensing by asymmetric dielectric gratings with both bound states in the continuum and guided mode resonances. Opt Express 2021;29:42978.

[47] Wang Q, Jiang JX, Wang L, Yin XY, Yan X, Zhu A, et al. An asymmetric grating refractive index sensor generating quasi-bound states in the continuum with high figure of merit and temperature self-compensation. J Phys D: Appl Phys 2022;55:155103.

[48] Koshelev K, Lepeshov S, Liu M, Bogdanov A, Kivshar Y. Asymmetric metasurfaces with High-Q resonances governed by bound states in the continuum. Phys Rev Lett 2018;121:193903.